J. Fluid Mech. (2009), *vol.* 634, *pp.* 217–243.
doi:10.1017/S0022112009007216 Printed in the United Kingdom

An experimental investigation of divergent bow waves simulated by a two-dimensional plus temporal wave marker technique

MOSTAFA SHAKERI, MOHAMMADREZA TAVAKOLINEJAD AND JAMES H. DUNCAN†

Department of Mechanical Engineering, University of Maryland, College Park, MD 20742, USA

(Received 19 March 2008 and in revised form 19 March 2009)

Divergent ship bow waves were simulated experimentally with a two-dimensional wavemaker that employs a flexible wave board. The wavemaker was programmed so that the wave board created a time sequence of shapes that simulated the line of intersection between one side of the hull of a slender ship model moving at constant speed and an imaginary vertical plane oriented normal to the ship model track. The time history of the water surface shape was measured with a cinematic laser-induced fluorescence technique for eight Froude numbers ($F_D = U/\sqrt{gD}$, where U is the forward speed of the equivalent three-dimensional ship model, g the acceleration of gravity and D the ship model draft). The waves produced ranged from small-amplitude non-breaking waves at the lowest Froude numbers to plunging breakers at the highest Froude numbers. These waves are strongly forced and at the higher Froude numbers begin breaking before leaving the wave board. The time histories of various geometric characteristics of the water surface shape including the hull contact line, the wave crest, the plunging jet and the splash zone, which is here defined as both the turbulent zone on the front face of the wave in the spilling breakers and the turbulent zone generated ahead of the jet impact point in the plunging breakers, were measured. The phase speed of the primary wave generated during each run ranged from $2.56U_{wl}$ (where U_{wl} is the maximum speed of the wave board at the undisturbed water level in the tank) at the lowest Froude number to about $1.7U_{wl}$ at the three highest Froude numbers. The maximum heights of the primary wave, the contact point on the wavemaker and the splash zone increased in a nearly linear fashion with increasing F_D. In the cases with plunging jets, the jet tip trajectory was parabolic with a vertical acceleration ranging from $0.6g$ at $F_D = 1.467$ to $0.8g$ at $F_D = 1.817$ (the highest Froude number).

1. Introduction

Breaking waves occur near the bows of ships moving at sufficient speed in calm seas. The character of the breakers depends on many factors including the speed of the ship, the shape of the hull and the distribution of weight in the ship. These breaking waves have a number of important consequences. First, the breakers convert energy from the mean flow into energy in the turbulent flow in the momentum-deficient wakes

† Email address for correspondence: duncan@umd.edu

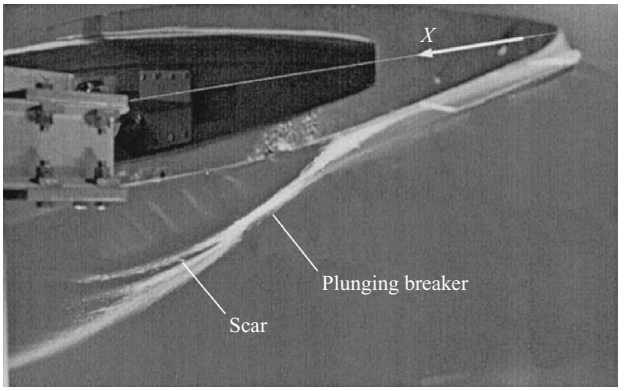

FIGURE 1. Bow-wave pattern around a ship model with a length of 3.05 m, $F_L = U/\sqrt{gL} = 0.446$, where U and L are the model speed and length and g is the acceleration of gravity. Aluminium powder was spread on the water surface. The camera was mounted on the towing carriage and set for an extended exposure. Adapted from figure 6(b) of Dong *et al.* (1997).

left behind the breakers. Baba (1969) has shown that up to 15 % of the resistance on some hull forms is associated with the wakes of breaking bow waves. Second, the breakers entrain air bubbles into the flow. These bubbles create underwater sound that can interfere with ship-board sonar and make the ship more detectable via passive sonar systems on other ships or platforms. The long bubbly wakes associated with the breakers are also detectable by various means from the air and via active sonar from below the surface.

The wave-breaking patterns of ship models have been visualized by many authors (see for example Miyata & Inui 1984; Dong, Katz & Huang 1997; Olivieri *et al.* 2007). Figure 1 which is from Dong *et al.* (1997) shows an extended exposure photograph (camera mounted on the towing carriage) of the breaking bow wave of a ship model, designated 4817 at the Naval Surface Warfare Center, Carderock Division (NSWCCD), model length $L = 3.05$ m, moving with length-based Froude number ($F_L = U/\sqrt{gL}$) of 0.446. At this Froude number, a plunging breaking bow wave is formed. The dark scar marked in the figure is bounded by a white bubble trail closer to the ship hull that is a result of air entrapped by the plunging bow wave. The white band below the dark scar is due to aluminium powder and bubbles in the water splash zone created outboard of the plunging jet impact. The authors reported that no air entrainment occurs at the lower Froude numbers used in their study (0.167, 0.279 and 0.334). Figure 2(a) which is from Olivieri *et al.* (2007) is an instantaneous image of the breaking bow wave from a test with a geosim ($L = 5.72$ m) of the 5415 model from NSWCCD, operating at $F_L = 0.35$ in a towing tank filled with sea water (salinity $\approx$30 parts per thousand). The turbulent splashing zone of the breaker is clearly visible as are streak structures within the splash zone. Two scars (nearly streamwise lines of minimum surface elevation) are visible, the first from the plunging jet impact and the second from the impact of the splash created by the first jet impact.

Ship wave field measurements have been reported by many investigators. The primary methods of measuring the wave pattern generated by ship models are visual estimation of the water contact line height distributions from photographs and records of water surface height versus time from fixed wire gauges as the model passes by. The closest possible fixed wire gauge position relative to the ship model is a little farther from the centreline than the half-beam of the model; otherwise the probe would

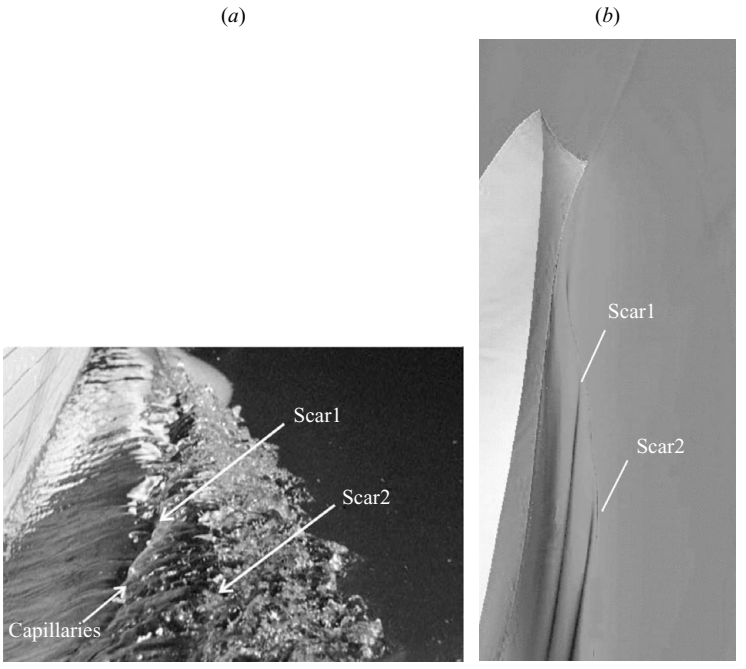

FIGURE 2. (*a*) Photograph of the wave field in an experiment with a model of the 5512 hull form at $F_L = 0.35$ (model length 3.05 m). (*b*) RANS calculation of the wave field of the 5512 hull form at $F_L = 0.35$. Photograph and calculations from Olivieri *et al.* (2007).

be struck by the model. Both of the above methods produce accurate profiles with low spatial resolution and little or no ability to measure fine details of breaking bow waves. A less routinely used method of measuring the wave field is the 'whisker probe' which is a conductivity probe that oscillates up and down via a servo mechanism, recording the vertical position of the probe when it first touches the water surface on each downward stroke. The probe can move with the model and so can measure the mean and the root mean square (r.m.s.) surface height throughout the bow region at high spatial resolution. In Olivieri *et al.* (2007), it was found that the regions of high r.m.s. surface height fluctuations correspond well to the breaking regions of the waves as seen in photographs. From the mean water surface height measurements, it was also possible to identify the scar structures mentioned above.

In recent years, investigators have explored breaking bow waves with three-dimensional numerical calculations and two-dimensional time-evolving numerical calculations called 2D+T methods. Three-dimensional calculations have been reported with both plunging and spilling breaking bow waves and numerical techniques include Reynolds-averaged Navier–Stokes (RANS; Olivieri *et al.* 2007) and volume of fluid (Dommermuth *et al.* 2006, 2007) methods. As an example of these calculations, figure 2(*b*) (also from Olivieri *et al.* 2007) shows mean surface height encoded as grey level for the same hull form and conditions as in the photograph in figure 2(*a*). The scars seen in the photograph are also visible in the numerical results. In the 2D+T method, the three-dimensional bow flow is approximated by a two-dimensional, time-evolving flow in which the hull is replaced by a deforming wall which at any time t ($t = 0$ is the time of passage of the stem at the mean water level) takes on the shape of the cross-section of one side of the hull at the streamwise (x) location corresponding

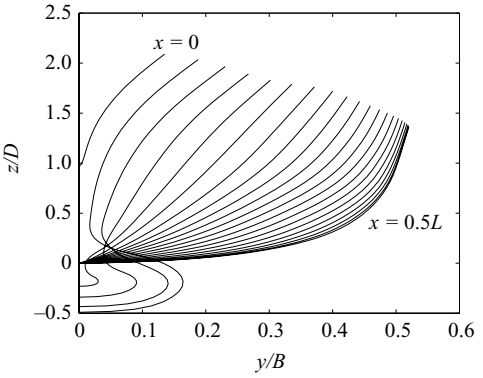

FIGURE 3. Vertical cross-sections of the model 5415 hull form at 20 equally spaced intervals from the stem to midships. The length, draft and beam of the model are given by L, D and B, respectively.

to $x = Ut$, where U is the equivalent speed of the three-dimensional ship model. The method is applicable only to ships with fine bows, and an approximation to the divergent wave components is produced. The accuracy of the 2D+T approximation is expected to increase with increasing Froude number. This method has been used by Tulin (1957) in high-speed planing flows, Tulin & Hsu (1986) in high-speed slender displacement hull flows, Song & Maruo (1993) in deck wetness flows and Tulin & Wu (1996), and Landrini, Colagrossi & Tulin (2001) in bow-wave flows. The numerical methods used in 2D+T calculations have included both boundary element potential flow methods and smooth particle hydrodynamics methods. In results using the latter method, the main features of the breaking waves are clearly seen.

The results presented in this paper are part of a larger study aimed at exploring the physics of air entrainment in breaking bow waves. In order to produce large energetic waves (wavelengths of the order of 2 m) with fairly realistic air entrainment in a facility in which long-term detailed experiments could be undertaken in salt water, a wave tank (14.8 m long, 1.15 m wide and 2.2 m deep) with a 2D+T wavemaker (keel depth 0.91 m) was constructed. In the present study, an approximation to the NSWCCD 5415 ship model was simulated with the 2D+T wavemaker. Profiles of the 5415 hull form from the stem to midships are shown in figure 3, and data files giving the full hull shape can be found at http://www.dt.navy.mil/hyd/sur-shi-mod/mod-5415-geo/index.html. The bulbous bow seen below the keel depth in figure 3 was removed in the 2D+T experiments, since its blunt nose violates the assumptions of the 2D+T approximation. In this first part of the investigation of these breaking waves, results from cinematic laser-induced fluorescence (LIF) measurements of the wave profiles are presented. As is shown below, these measurements are able to capture detailed features of the breaking process. There are no corresponding measurements of the waves produced by the three-dimensional 5415 ship model modified to exclude the bulbous bow. Thus, no direct comparison between the waves generated by the 2D+T wavemaker and three-dimensional ship model experiments can be made. However, comparisons between wave measurements in a three-dimensional ship model experiment using a model that does not have a bulbous bow (NSWCCD model 5365) at the NSWCCD and a 2D+T approximation to this ship model performed in the present wave tank showed good agreement in wave height and shape at high Froude numbers (Shakeri *et al.* 2009).

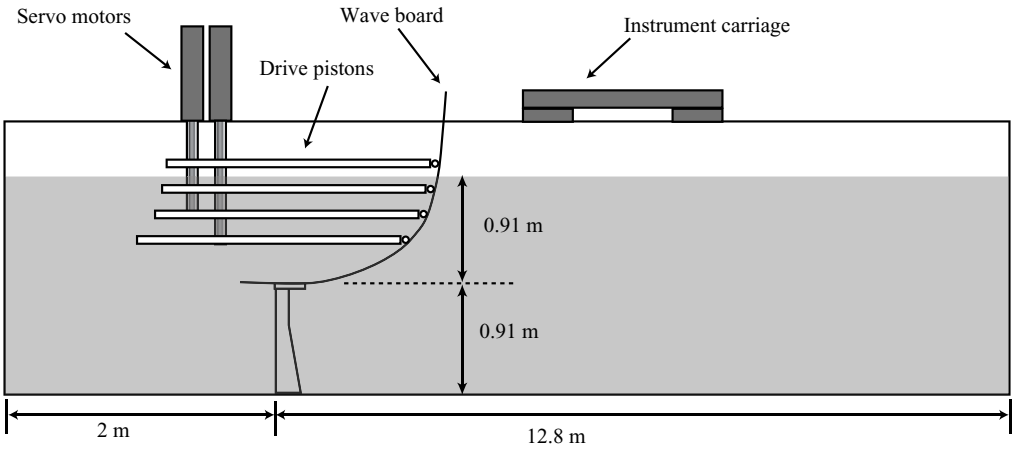

FIGURE 4. Schematic drawing showing the tank, 2D+T wavemaker and instrument carriage. The tank is 14.8 m long, 1.15 m wide and 2.2 m deep.

The remainder of this paper is divided into three sections. In § 2, the test facilities and wave measurement techniques are described. The results of the wave measurements are presented and discussed in § 3. Finally, the conclusions are given in § 4.

2. Experimental details

2.1. *The wave tank*

The experiments were carried out in a wave tank that is 14.80 m long, 1.15 m wide and 2.20 m deep (water depth 1.83 m). A schematic of the wave tank is shown in figure 4. The inside surface of the tank consists of a set of large flat panels which are in turn supported by a superstructure consisting of steel beams. All of the floor panels and the wall panels at the two ends of the tank are made of 0.635 cm thick stainless steel plates, while the panels on the long sidewalls of the tank are made of 3.5 cm thick clear acrylic.

The 2D+T wavemaker occupies about 2.8 m of the tank length at one end. This leaves about 12 m from the retracted position of the wave board (the midplane of the equivalent three-dimensional ship model) to the far end of the tank. The travel time for waves generated by the wavemaker to reach the far end of the tank and return to the measurement site limits the length of time in which uncontaminated measurements can be made. In the experiments discussed herein, it is important that the wave reflection time (ΔT_R) is longer than the time (ΔT) between the passage of the bow and that of the middle of the equivalent three-dimensional ship model:

$$\Delta T = \frac{L}{2U} = \frac{1}{2F_L}\sqrt{\frac{L}{g}}, \tag{2.1}$$

where g is gravity; L (=21.03 m, see below) is the equivalent three-dimensional ship model length; U is the equivalent three-dimensional ship model forward speed; and $F_L = U/\sqrt{gL}$ is the Froude number (see table 1). Using the above equation at an equivalent full-scale speed of $U_s = 27.5$ knots (the fastest equivalent ship speed for the tests described herein, $F_L = 0.379$) and $U_s = 12.5$ knots (the slowest ship speed for the experiments described herein, $F_L = 0.172$) we find $\Delta T = 1.93$ s and $\Delta T = 4.25$ s, respectively. The highest possible surface wave speed in water of depth H is the

U_s (knots)	U (m s^{-1})	T_{wm} (s)	U_{wl} (m s^{-1})	F_L	F_D	X_B (m)	T (m)	α_E (deg.)	F_T
12.5	2.473	4.480	0.594	0.172	0.826	3.381	0.615	9.60	1.007
15.0	2.968	3.733	0.713	0.207	0.991	3.734	0.608	9.97	1.216
16.5	3.264	3.393	0.784	0.227	1.090	3.825	0.606	10.06	1.339
17.5	3.462	3.200	0.831	0.241	1.156	3.949	0.604	10.17	1.423
20.0	3.957	2.800	0.950	0.276	1.321	4.389	0.597	10.47	1.635
22.5	4.452	2.489	1.069	0.310	1.487	4.591	0.594	10.57	1.844
25.0	4.946	2.240	1.188	0.344	1.652	4.830	0.592	10.67	2.052
27.5	5.441	2.036	1.307	0.379	1.817	5.060	0.590	10.73	2.262

TABLE 1. Table of experimental conditions. Symbol definitions: U_s, full-scale ship speed; U, equivalent three-dimensional ship model speed; T_{wm}, wavemaker run time (i.e. time for half the equivalent ship model length to pass a fixed observer, $T_{wm} = 0.5L/U$); U_{wl}, maximum horizontal speed of the wave board at the undisturbed water level; F_L, Froude number based on model (or ship) length ($F_L = U/\sqrt{gL} = U_s/\sqrt{gL_s}$, where L_s is the ship length and L is the model length); and F_D, Froude number based on model (or ship) keel depth ($F_D = U/\sqrt{gD} = U_s/\sqrt{gD_s}$, where D_s is the ship keel depth and D is the model keel depth). For the 2D+T model, $L = 21.03$ m, $D = 0.914$ m, $B = 2.82$ m and $U = 4.165U_{wl}$. The last four columns are quantities involved in comparison with the theoretical results of Noblesse *et al.* 2008 (see figure 15*b*): L_B, the equivalent streamwise distance from the stem to the maximum height of the contact line; T, the equivalent draft in the bow region; α_E, the equivalent bow entrance angle; and $F_T = U/\sqrt{gT}$.

shallow-water wave speed $\sqrt{gH}$ which equals 4.24 m s^{-1} for the present case with $H = 1.83$ m. This is both the energy and the phase speed of a wave whose length is many times greater than the water depth. At this speed, a wave can traverse the 24 m long distance from the wavemaker to the far end of the tank and back in a time of $\Delta T_w = 5.66$ s which is longer than ΔT, even at the slowest equivalent three-dimensional ship model speed. It should also be emphasized that waves with lengths much greater than the water depth did not have significant amplitude in the present experiments and that the typical wave length generated was about 2 m. This wavelength has a group velocity of 0.88 m s^{-1} and so a much longer reflection time than the shallow-water waves. The above analysis shows that wave reflections do not influence the present measurements.

2.2. *The 2D+T wavemaker*

A schematic drawing of the 2D+T wavemaker is shown in figure 5, and a schematic drawing showing its installation in the wave tank is given in figure 4. The wavemaker is powered by four servomotors, which, through gear reducers, drive four vertically oriented shafts. Each shaft drives a toothed pulley, which drives a piston through a rack-and-pinion system. The pistons drive horizontally oriented plates that are as wide as the tank (1.14 m) and are guided along the tank walls by tracks. Position sensors and motor-shaft optical encoders are used in a computer-based feedback-control system to achieve the desired motion of each piston. The frame of the 2D+T wavemaker is bolted to the bottom and sidewalls of the tank. Most of the device is submerged and is made of appropriate materials to resist corrosion.

The main component of the 2D+T wavemaker is the flexible wave board which is attached to the four drive plates via hinges. The wave board, which spans the width of the wave tank with a clearance of about 1.5 mm on each side, is constructed from interleaved 1.6 mm thick stainless steel plates of various lengths. The plates are slotted and riveted together in a way that does not allow any flow of water through

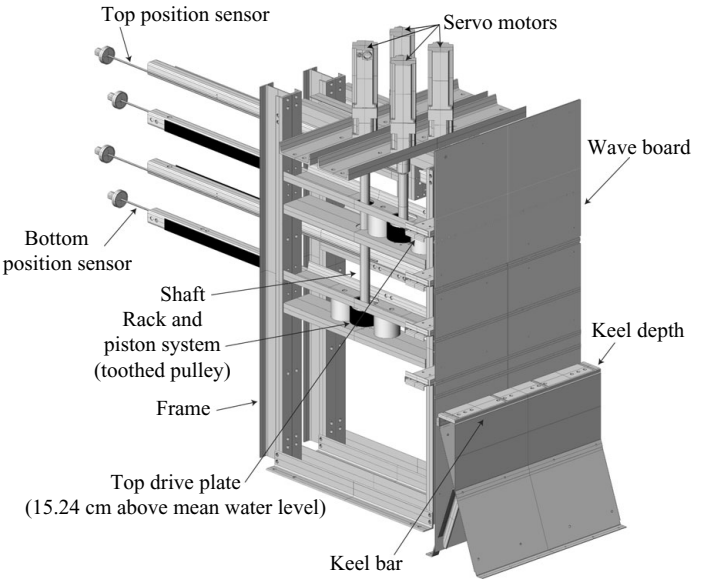

FIGURE 5. A schematic drawing of the 2D+T wavemaker. This device was designed and manufactured by MTS Systems Corporation.

the wave board via a straight path, other than the thin gaps between the wave board and the tank sidewalls. The stainless steel plates are thin enough to bend elastically under the differential action of the drive plates. Each drive plate is attached to a different layer of stainless steel so that as the pistons move out at different speeds, the changing distance between the hinge points is accommodated by the stainless steel plates sliding relative to each other. The keel depth of the 2D+T wavemaker is created by bending the wave board over a fixed horizontal surface, called the keel bar, that spans the width of the tank at 0.91 m above the floor of the tank (see figures 4 and 5). The keel bar is supported by a steel structure which is bolted to the floor of the tank. A delrin block forms the top surface of the keel bar, where it comes in contact with the wave board. The mean water depth is fixed at 0.914 m above the top surface of the keel bar, thus creating the keel depth for the wavemaker and equivalent three-dimensional ship model. The beam-to-draft ratio of the 5415 model is 3.085, and the length-to-draft ratio is 23.01. Thus, with a draft of 0.914 m, the half-beam of the 2D+T model and the equivalent three-dimensional model is 1.410 m, and the equivalent three-dimensional model length is 21.03 m. Further details on the 2D+T wavemaker can be found in Shakeri (2005) and Shakeri *et al.* (2009).

The 5415 hull profile was modified in two ways for use in the 2D+T simulations. First, the bulb that appears below the model keel depth was removed. This is necessary, since the 2D+T approximation requires a slender bow, while the bulb has a very blunt profile. Second, the stem region of the 5415 hull form was modified as is explained below. Figure 6(*a*) shows a plan view of the stem region at the mean water line. As can be seen in the figure, the stem of the 5415 hull shape has a small rounded nose. Simulation of this nose shape with the 2D+T wavemaker would require the wave board to accelerate from zero to finite speed in one wavemaker control time step. When the wavemaker attempts to create this motion it sets up an oscillation in the velocity of the drive channels, and this in turn creates short wavelength surface

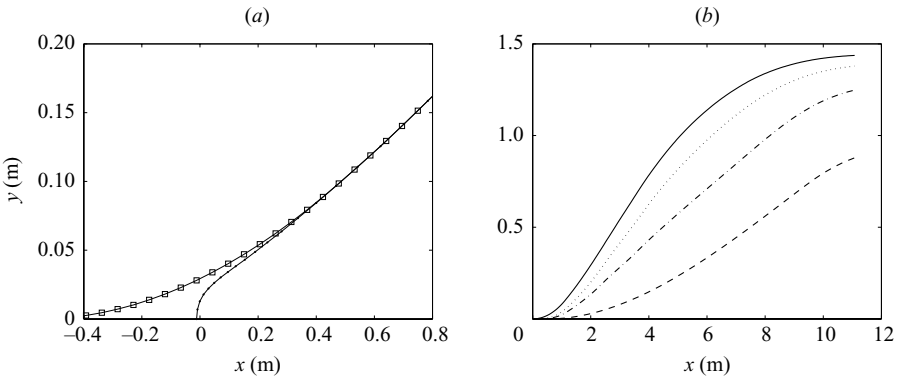

FIGURE 6. Profiles of the 5415 hull form in the horizontal (x–y) plane. (a) Profile of the starboard side of the stem region of the 5415 hull form at the water line and the approximation to it used in the 2D+T wavemaker: ●, water line profile of the 5415 hull form; □, water line profile of the equivalent hull form used by the 2D+T wavemaker. (b) Profiles of the starboard side of the 5415 model from stem to midships at the elevations of the four drive channels of the 2D+T wavemaker. The wavemaker input signals are obtained by converting the horizontal axis to time via the transformation $t = x/U$: —, drive channel 1 (top, 15.2 cm above the mean water level); · · · · ·, drive channel 2 (15.2 cm below the mean water level); – ·– · –, drive channel 3 (45.7 cm below the mean water level); — — —, drive channel 4 (bottom, 76.2 cm below the mean water level).

waves. To remedy this problem the rounded stem was replaced with the sharp stem created from a third-order polynomial as shown in figure 6(a).

Profiles of the wavemaker input to the four drive channels are given in figure 6(b). Measurement of the time histories of the positions of the four drive channels for three runs at the highest equivalent ship speed indicates that the wavemaker reproduces these profiles with an r.m.s. error of at most 6 mm during the piston displacements which range from 1.44 m for the top drive channel to 0.87 m for the bottom drive channel. The corresponding run-to-run repeatability of the wavemaker drive channel motion was within ± 0.8 mm r.m.s. at any instant during a run. Side-view high-speed movies of the wave board were also taken for all experimental conditions used in this study. These movies were analysed to obtain the wave board shape versus time. The data for equivalent full-scale ship speeds of 20.0 and 27.5 knots can be found at journals.cambridge.org/flm.

2.3. *The instrument carriage*

In order to make measurements in a reference frame moving with the top drive channel of the wavemaker, an instrument carriage and towing system was designed and constructed. Figure 4 shows a schematic of the wave tank including the instrument carriage. This system consists of the drive assembly, cables, tracks, instrument carriage and position sensor. The carriage is controlled by the same computer and software that control the wavemaker.

The carriage is powered by a servomotor and wire rope system. The carriage is supported by four hydrostatic oil bearings that ride on precision rails, one on either side of the tank. When high-pressure oil is supplied to the bearings, a thin film of oil is forced between the bearings and the tracks. This oil layer dramatically reduces vibration and friction levels when the carriage is in motion. Precise motion profiles for the carriage are obtained by the same means used for the drive channels of the wavemaker. Position feedback is provided by a precision position sensor that

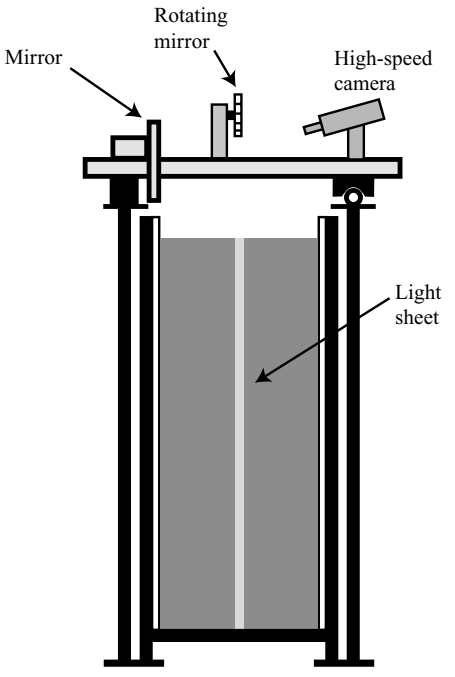

FIGURE 7. Schematic of the wave tank and imaging system. End view looking away from the wavemaker. The water is mixed with fluorescent dye.

is attached to the tank and extends over the length of travel of the carriage. The position sensor readings are used by the carriage control software to obtain precise repeatable carriage motions. The maximum speed and acceleration of the carriage towing system are $3.1\,\mathrm{m\,s^{-1}}$ and $6\,\mathrm{m\,s^{-2}}$, respectively.

2.4. *The water treatment*

At the beginning of each experiment, the tank was filled with filtered tap water, and hypochlorite was added at a concentration of 10 ppm to neutralize organic materials. A water circulation and skimming system was then used for a period of time to further purify the water. In this system, the tank water is removed through a surface skimmer at the end of the tank farthest from the wavemaker. The cleaned water is then pumped through a diatomaceous filter and back into the wave tank at the end near the wavemaker. Just before the wave experiments begin, the free chlorine level in the tank is reduced to zero by addition of an appropriate amount of hydrogen peroxide, and a fluorescent dye is mixed with the water for visualization purposes. The reduction in chlorine level is necessary to preserve the dye. The water skimming and filtration system was turned on during the time between experimental runs in order to minimize the level of naturally occurring surfactants in the wave tank.

2.5. *Wave measurements*

A schematic layout of the set-up for the wave profile measurements is shown in figures 7 and 8. The purpose of the system is to record the surface profile at the centre plane of the tank in a moving reference frame. The measurement system has three main components: a light source, optics and a high-speed digital camera. Each component is discussed below.

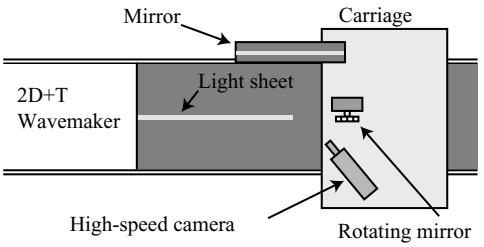

FIGURE 8. Schematic of the wave tank and imaging system. Top view.

The light source for the imaging system is a 7 Watt argon ion laser (Coherent Innova 90) operating in all lines mode. The laser is mounted on a table next to the wave tank at the end with the wavemaker. The beam is directed horizontally towards the far end of the tank. A number of optical components are used to manipulate the laser beam between the laser and the water surface. A set of three mirrors is used to redirect the beam so that it points horizontally from above the wavemaker towards the carriage and in the centre plane of the tank. The last two mirrors are used to adjust the direction of the beam so that it hits the optics on the carriage in the same spot regardless of the carriage position as it moves along the tank. Two spherical lenses placed between the first two mirrors in the optical path are used to focus the beam on to the water surface. According to the paraxial ray approximation analysis, the minimum thickness of the laser beam at the water surface is 2 mm. It should be noted that as the carriage moves, the distance along the optical path between the laser and the water surface changes, and so does the thickness of the beam at the water surface. Thus, the focal point of the system was set to be about halfway between where the carriage starts and ends its motion.

In order to convert the circular laser beam into a light sheet, a rotating 12-sided polygon with mirrored surfaces was mounted on the instrument carriage with its axis of rotation horizontal and perpendicular to the direction of the laser beam. As the polygonal mirror rotates, the reflected beam translates over an angle of 60° ($2 \times 360°/12$) in the vertical centre plane of the wave tank. The mirror rotates at about 12 000 rpm during a typical exposure of about 4 ms for each image of the high-speed camera (see discussion below); the laser scans the field of view about 10 times and appears to the camera as a uniform light sheet. The span of the light sheet at the water surface was set to about 0.8 m by adjusting the heights of the laser beam and the rotating mirror. The angle between the centreline of the light sheet and the undisturbed water surface was set to about 45° by adjusting the height of the rotation axis of the mirror relative to the height of the laser beam.

The intersection of the light sheet and the water surface was photographed with a high-speed digital camera (Phantom v9, Vision Research) which was mounted on the instrument carriage. The camera was set to record 1632×1200 px images with 8 bit grey levels at a frame rate of 256 images per second. The water was mixed with fluorescein dye at a concentration of 2–3 ppm. A long-wavelength-pass colour filter was placed in front of the camera lens in order to block any specular reflections of laser light. The camera viewed the water surface through a long flat mirror which was also mounted on the carriage (see figures 7 and 8). The viewing direction of the camera relative to the normal to the light sheet was about 30°. This relatively large angle was required to get a clear view of the front face of the wave and to avoid accidental collisions of the wave board and the instrument carriage during the experiments.

FIGURE 9. A photograph of the calibration chequerboard with its surface in the plane of the light sheet.

Movies taken by the high-speed camera were transferred to a desktop computer for processing. Each movie carries about 6 s of the wave generation process, containing about 1600 images. Gradient-based image processing techniques programmed in MATLAB were used to extract the profile of the wave from each image.

Since the camera viewed the wave profile from a relatively large angle to the light sheet, the images show a distorted view of the wave profiles and must be transformed before any further processing. For this purpose, a black-and-white chequerboard pattern with 2.54 cm squares that was 61.0 cm high and 243.8 cm long was printed, laminated and taped to a flat plastic board that was mounted on an aluminium frame. Before any set of experiments, the chequerboard target was placed in the plane of the light sheet with its far end in contact with the wave board, and a picture of the chequerboard was taken with the high-speed movie camera. A sample calibration image is given in figure 9. These calibration images were then used to transform points in the image plane into the physical plane (plane of the light sheet), via an interpolation technique. The field of view at the mean water line is about 0.8 m in each image, yielding a resolution of about $2\,\mathrm{px\,mm^{-1}}$. In regions of the wave profile in which the water surface is smooth, considering errors in image calibration, locating the water surface in the images and determining the carriage position when the image is taken, it is estimated that points on the water surface can be determined to an accuracy of ± 1.3 mm in the physical plane. In regions of the wave profile in which the surface is rough and ill defined due to air entrainment, the accuracy is estimated to be ± 5 mm.

As mentioned above, the camera is mounted on the instrument carriage which is programmed to move with the top drive channel of the wavemaker. In order to determine the water surface shape in laboratory coordinates at each moment during the wavemaker motion, the positions of the four drive channels of the wavemaker and the carriage must be known at the time each wave profile image is taken. This synchronization was accomplished in the following manner: First, a computer records the positions of all four drive channels and the instrument carriage at the sampling rate of the camera, 256 Hz. Thus, there is a set of positions recorded for each image. In order to synchronize the records of the computer and the camera, the computer was programmed to send a trigger signal to a function generator that then began sending a 256 Hz signal to the camera to control the time at which each image was taken. In order to relate the frame number in the high-speed movies to the wavemaker and carriage position readings recorded by the computer, images of a fixed point were used. To this end, the camera was set up to record images of a vertical line that was

marked on the sidewall of the tank. With the carriage stationary, the carriage position sensor reading and the column of pixels corresponding to the vertical mark in the camera image were recorded. Then, during an experimental run of the wavemaker and carriage, the image number in which the mark was at the recorded pixel column was noted, and the line of position data in the computer record with the corresponding carriage position was found. In this way the synchronization was achieved.

2.6. *Test procedure and conditions*

The series of tests to measure the water surface profiles for one equivalent ship speed takes about one day of laboratory time. The steps taken each day to obtain these measurements are given below. During this period, the water depth was monitored and held constant to ensure that the depth-based Froude number did not change. Also, the water surface in the tank was kept clean by running the skimming system all day with the exception of a short period before and during each experimental run.

Before any set of experiments, the calibration board was placed in the plane of the laser light sheet, and a calibration image was taken. A second image of the calibration board was also taken at the end of each day of experiments. For each equivalent ship speed, several movies were taken with the carriage moving but the wavemaker turned off. These movies were used to obtain the mean water surface in each image.

The waves were generated with the 2D+T wavemaker at eight different equivalent ship speeds U_s: 12.5, 15.0, 16.5, 17.5, 20, 22.5, 25 and 27.5 knots. The equivalent three-dimensional ship model speed (U), the wavemaker run time (T_{wm}), the maximum speed of the wave board at the undisturbed water level (U_{wl}, taken as the average of the maximum speeds of the top, 15.2 cm above the undisturbed water level, and second, 15.2 cm below the undisturbed water level, drive channels of the wavemaker) and the Froude numbers based on ship or model draft (F_D) and ship or model length (F_L) for each of these equivalent ship speeds are given in table 1. In the remainder of this paper, each condition will be referred to by its value of F_D. Since the wave pattern created by the wavemaker can reach a width of about 2.8 m at the time of passage of the stern of the equivalent three-dimensional ship and since the camera field of view was only about 0.8 m, multiple runs with the carriage motion starting at different distances from the wavemaker were required to measure the entire wave pattern for a single equivalent ship speed. These movies were labelled by the zone number – there were four zones, and zone 1 was closest to the wavemaker. The measurements in each zone were, of course, performed in separate experimental runs, and each run was repeated at least three times.

3. Results and discussion

The experimental results are presented below in three subsections. First, the general characteristics of the breaking waves are discussed with the aid of images from the high-speed movies in § 3.1. Next, in § 3.2, features of the overall wave field are discussed. Finally, in § 3.3, time histories and trajectories of various geometrical features are presented and discussed.

3.1. *Qualitative observations*

The eight experimental conditions given in table 1 can be broken into three Froude number ranges according the behaviour of the waves that are generated. Non-breaking waves were generated at $F_D = 0.826$ and 0.991; spilling breakers were generated at $F_D = 1.090$, 1.156 and 1.321; and plunging breakers were generated at $F_D = 1.487$, 1.652 and 1.817. Figures 10–12 contain images from the high-speed LIF movies of

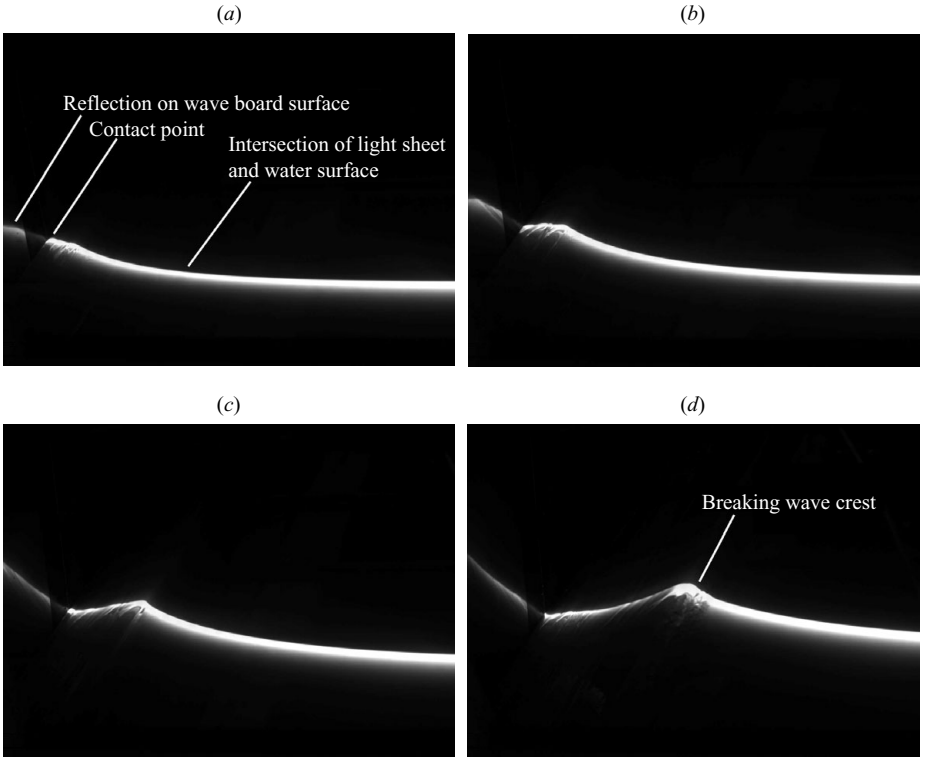

FIGURE 10. LIF images from high-speed movies of the wave formation process at four different times for $F_D = 1.090$ ($U_s = 16.5$ knots). A weak spilling breaker is generated: (*a*) $t = 0.346$ s ($0.102T_{wm}$), (*b*) $t = 0.458$ s ($0.135T_{wm}$), (*c*) $t = 0.578$ s ($0.170T_{wm}$) and (*d*) $t = 0.763$ s ($0.225T_{wm}$); $T_{wm} = 3.393$ s. These images were taken in a reference frame that is nearly fixed with respect to the top drive channel (located 15.24 cm above the mean water level) of the wave board. The contact point is the intersection of the wave board and the water surface in the plane of the light sheet. The horizontal field of view of each image is about 0.8 m.

experimental runs with $F_D = 1.090$ (the weakest spilling breaker), 1.321 (the strongest spilling breaker) and 1.817 (the strongest plunging breaker), respectively. All the images in figures 10 and 11 and the first three images in figure 12 were taken with the carriage in the zone 1 position relative to the wave board, which is located on the left side of the images. In the last image in figure 12(*d*), the carriage is in the zone 2 position, and the physical position of the wave board is 0.625 m to the left of the physical point, corresponding to the left edge of the image at the water surface. It should be kept in mind that these images show a distorted view of the wave due to the large camera angle relative to the plane of the light sheet. This distortion is evident in the sample image of the calibration chequerboard shown in figure 9.

The high-contrast boundary between the black region on the top of each image and the lighter region on the bottom is the intersection of the laser light sheet and the water surface. The light source for the intensity pattern below this high-contrast boundary is the glowing dye within the subsurface portion of the light sheet. This light either serves to illuminate features like the portion of the plunging jet between the camera and the light sheet as seen in figure 12 or creates a varied intensity pattern as the subsurface light sheet is viewed through the curved water surface.

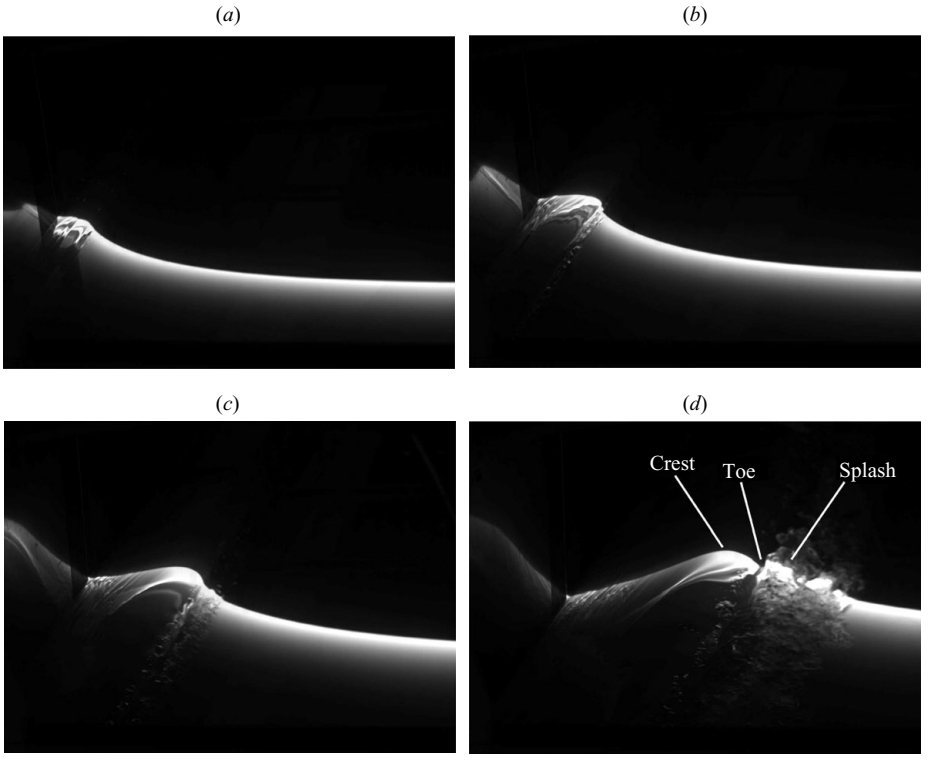

FIGURE 11. LIF images from high-speed movies of the wave formation process at four different times for $F_D = 1.321$ ($U_s = 20.0$ knots). A strong spilling breaker is generated: (*a*) $t = 0.346$ s ($0.124T_{wm}$), (*b*) $t = 0.458$ s ($0.164T_{wm}$), (*c*) $t = 0.578$ s ($0.206T_{wm}$) and (*d*) $t = 0.763$ s ($0.273T_{wm}$); $T_{wm} = 2.800$ s. These images were taken in a reference frame that is nearly fixed with respect to the top drive channel (located 15.24 cm above the mean water level) of the wave board. The horizontal field of view of each image is about 0.8 m.

In all three figures, the selected photographs were taken at $t = 0.346$, 0.458, 0.578 and 0.763 s after the start of the wavemaker motion. When non-dimensionalized by the wavemaker run times (T_{wm}; see table 1 for values), the dimensionless times corresponding to the images in figure 10 are $t/T_{wm} = 0.102$, 0.135, 0.170 and 0.225, and those corresponding to the images in figure 12 are $t/T_{wm} = 0.170$, 0.225, 0.280 and 0.375. Thus, the last two images in figure 10 and the first two images in figure 12 were taken at the same dimensionless times.

The images in figure 10 were taken with the wavemaker operating at a Froude number of $F_D = 1.090$, the lowest Froude number for which wave breaking was observed. In figure 10(*a*), the water surface at the contact point of the free surface on the wave board has risen by a small amount. To the right of the contact point, a few ripples can be seen; these ripples are generated by very slight oscillations in the velocity of the wave board during start-up. Further to the right, the water surface drops gradually to the undisturbed water level in the tank. In figure 10(*b*) the contact point has risen further, and there is a short flat section of water surface between the contact point and the point at which the surface begins a smooth drop to the undisturbed water surface further to the right. In figure 10(*c*), the contact point has fallen below its maximum height, and a wave crest can be seen. This crest is moving to the right and has just begun to break. In figure 10(*d*) the wave crest has moved

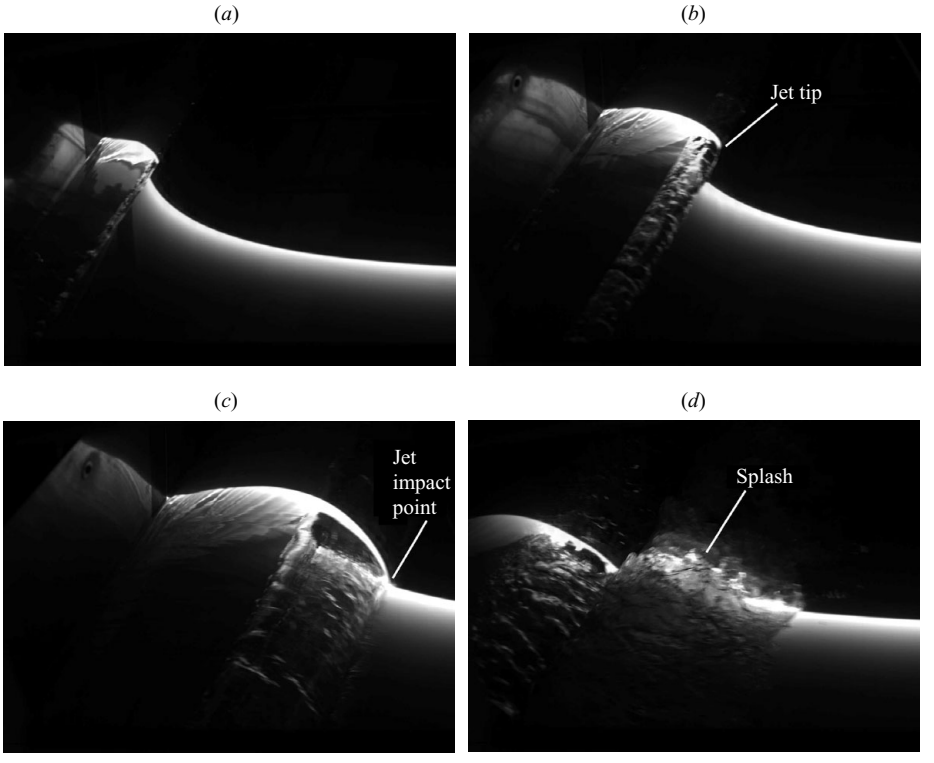

FIGURE 12. LIF images from high-speed movies of the wave formation process at four different times for $F_D = 1.817$ ($U_s = 27.5$ knots). A strong plunging breaker is generated: (*a*) $t = 0.346$ s ($0.170T_{wm}$), (*b*) $t = 0.458$ s ($0.225T_{wm}$), (*c*) $t = 0.578$ s ($0.280T_{wm}$) and (*d*) $t = 0.763$ s ($0.375T_{wm}$); $T_{wm} = 2.036$ s. These images were taken in a reference frame that is nearly fixed with respect to the top drive channel (located 15.24 cm above the mean water level) of the wave board. The horizontal field of view of each image is about 0.8 m.

further away from the wave board and has evolved into a fully turbulent spilling breaker. This process in which the contact point first rises and then falls at the time at which the main wave crest is ejected is seen at all Froude numbers.

In figure 11 ($F_D = 1.321$), a strong spilling breaker is formed. At the condition with the next highest Froude number (see table 1), a weak plunging breaker is formed. The sequence of events shown in figure 11(*a–d*) is quite similar to those found at $F_D = 1.090$ (see figure 10). However, at $F_D = 1.090$, breaking begins at about the time of figure 11(*c*) which was captured at $t = 0.170T_{wm} = 0.578$ s, while at $F_D = 1.321$, breaking begins before figure 11(*b*) which was captured at $t = 0.164T_{wm} = 0.458$ s. Thus, breaking begins at an earlier time measured either in seconds or in dimensionless units. Note also that at $F_D = 1.321$ breaking begins before the wave crest leaves the wave board. As can be seen in figure 11, a rather large region of rough water surface, herein called the splash zone, is created ahead of the sharp upward curvature point, herein called the toe, at the upstream (right) side of the bulge on the front face of the wave.

In figure 12 ($F_D = 1.817$), a strong plunging breaker is formed. In figure 12(*a*), the contact point has risen to a much greater height than it has at the same time in the slower-speed cases (figures 10*a* and 11*a*). To the right of the contact point, there is a short section of flat water surface followed by a plunging jet that is just beginning to form. In figure 12(*b*), the contact point has risen further; the water surface to

the right of the contact point is relatively flat; and the jet is more developed. In figure 12(*c*), the contact point has begun to drop, and the wave crest can be seen to the right of the contact point. The jet has evolved to the point of impact with the smooth water surface to the right. This jet impact creates a splash to the right of the impact point, and in figure 12(*d*) this splash is beginning to form in a manner similar to the spilling breaker seen at $F_D = 1.487$ (figure 11). A short time later, the wave crest disappears, and the highest point on the wave profile becomes the peak of the splash. All of the above-mentioned behaviour is similar to that reported by Bonmarin (1989) and Rapp & Melville (1990) for plunging breakers formed in open water.

It is interesting to note that the initiation of the breaking at $F_D = 1.090$ case and the impact of the plunging jet at $F_D = 1.817$ occur at about the same physical time, $t = 0.578$ s, relative to the start of the wavemaker motion. However, using the 2D+T transformation $x = Ut$, the jet impact in the high-speed case would occur at a larger streamwise distance from the stem of the equivalent three-dimensional model or ship.

Since the images in figures 10(*c*) and 12(*a*) ($F_D = 1.090$) and the images in figures 10(*d*) and 12(*b*) ($F_D = 1.817$) were taken at the same dimensionless times, $t = 0.170T_{wm}$ and $t = 0.225T_{wm}$, respectively, each pair of images corresponds to the same streamwise distance along the equivalent three-dimensional model or ship hull. As can be seen from the images, by $t = 0.225T_{wm}$ the wave for $F_D = 1.090$ is a fully formed spilling breaker, while the plunging jet found at $F_D = 1.817$ is in a relatively early stage of formation. In this high-speed case, a fully turbulent flow is formed at about the time of the image in figure 12(*d*), $t = 0.375T_{wm}$.

Although the motion of the wavemaker is two-dimensional, three-dimensionality begins to appear in the free surface in the splash zone found ahead of the toe after the spilling process starts in the slower-speed cases or after the jet formation process is well underway in the higher speed cases. In the plunging jet cases, this three-dimensionality appears first as ripples on the underside of the jet and the jet tip. A theory of the breakup of two-dimensional plunging jets was given by Longuet-Higgins (1995). In the present work, after jet impact, the flow becomes fully turbulent, and three-dimensional drops and bubbles form.

3.2. *Overall wave pattern*

Sequences of the measured wave profiles for $F_D = 1.090$, 1.321 and 1.817 are shown in figure 13(*a–c*), respectively. These profiles correspond to the conditions for the photographs shown in figures 10–12. The profiles are plotted in a manner that shows the 2D+T approximation to the ship model wave field. The horizontal axis is the dimensionless cross-stream distance (y/L) from the ship centre plane (which is also the retracted position of the wave board), and the vertical axis is both the dimensionless streamwise distance x/L and the dimensionless water surface height z/D. Each line in the plot is the wave profile ($0.1z/D$ versus y/L) plotted at some time t after the start of the wavemaker motion, and the $z = 0$ line for each profile is located at the vertical position $x/L = Ut/L$ in the plot. The white area on the left side of each plot is the plan view of the port side of the front half of the ship model as measured from the contact line to the midplane. It should also be mentioned that each plot was obtained from image sequences in zones 1–4 in four separate runs of the wavemaker. In areas in which the water surface is smooth, the profiles from adjacent zones match well in the overlap region. In areas in which the water surface is rough, the profiles do not match as well due to the changes in the profile from run to run that are caused by the random nature of the turbulence-induced small-scale features of the surface shape.

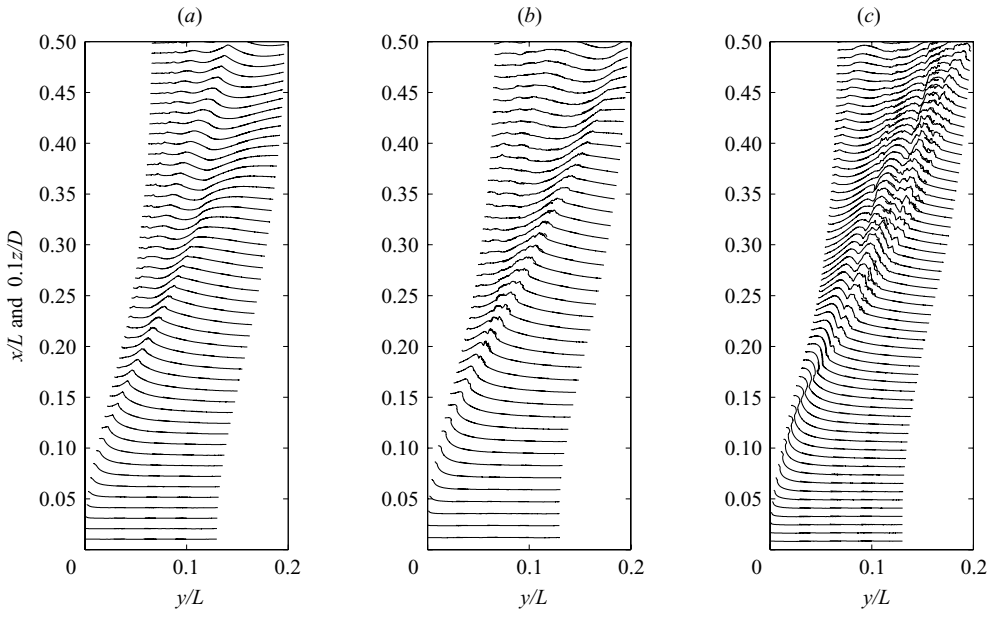

FIGURE 13. Profile histories of the divergent bow waves generated by the 2D+T wavemaker at Froude numbers of (*a*) $F_D = 1.090$, (*b*) $F_D = 1.321$ and (*c*) $F_D = 1.817$. Each wave profile is a plot of local dimensionless water surface height $0.1z/D$ versus cross-stream distance y/L at a streamwise distance given by the 2D+T approximation $x/L = Ut/L$; U, L and D are the speed, length and draft of the equivalent three-dimensional ship model. The spacing between the curves is $\Delta x/L = 0.0097$ in (*a*), $\Delta x/L = 0.0117$ in (*b*) and $\Delta x/L = 0.0081$ in (*c*).

The wave patterns are qualitatively similar to the patterns seen in most photographs of naval combatant ships moving at high speed, including the photographs of the wave fields around ship models shown in figures 1 and 2(*a*) and the calculated wave field in figure 2(*b*). This similarity includes both the locations of the wave crests and the locations of the breaking zones. The scar patterns seen in figures 1 and 2 are clearly visible as streaks of low elevation points at the higher Froude numbers in the 2D+T results. These features have also been found in the smooth particle hydrodynamics calculations of ship bow flows by Landrini *et al.* (2001).

3.3. *Geometrical parameters*

3.3.1. *Contact line*

Profiles of the dimensionless height of the water surface contact point on the wave board (z_c/D, measured from the undisturbed water surface) versus dimensionless time (t/T_{wm}) are shown in figure 14(*a*) for all eight Froude numbers. Using the 2D+T transformation $x = Ut$, these profiles would become the water line profiles frequently reported in three-dimensional ship model experiments. The 2D+T data for each Froude number were obtained from a single experimental run. For the highest Froude number, data were reduced for three experimental runs, and the results are plotted in figure 14(*b*), where it can be seen that the curves of z_c/D versus t/T_{wm} are highly repeatable. For all Froude numbers shown in figure 14, the contact point initially rises rapidly to its maximum height and then falls more slowly. This qualitative behaviour is typical of ship bow waves (see for example Noblesse *et al.* 2008). The time of the maximum value of z_c ranges from about $0.15T_{wm}$ to $0.25T_{wm}$ as F_D increases from 0.826 to 1.817. During the descent of the contact point after

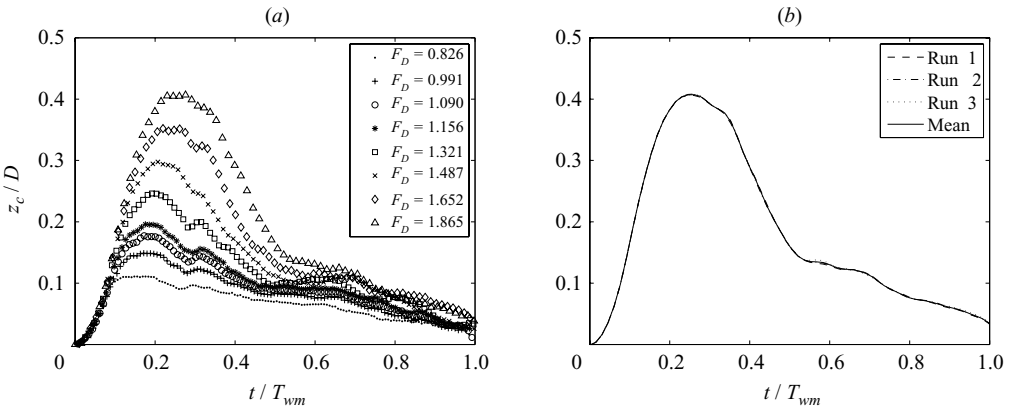

FIGURE 14. The height of the water contact point (z_c/D) versus time (t/T_{wm}). (*a*) Data from single experimental runs for all eight Froude numbers. (*b*) Data from three experimental runs at the highest Froude number, $F_D = 1.817$.

the maximum, there is a small peak which occurs consistently at $t/T_{wm} \approx 0.32$. For comparison, consider that the top two drive channels of the wavemaker reach their maximum speed at about $0.2T_{wm}$ and that this speed remains close to this highest value until about $0.35T_{wm}$ at which it begins to drop. Though there is no clear single feature in the drive channel velocity record to correspond with the maximum height of the contact line, it is clearly in the range of times when the drive channel reaches its maximum speed.

A plot of the maximum values of z_c/D versus F_D is given in figure 15. The maximum height increases monotonically with increasing Froude number, reaching $0.41D$ at $F_D = 1.817$. The data form a nearly straight line with a positive slope of about 0.3. No contact point height data for a three-dimensional ship model with the present hull shape (5415 model with the bulbous bow removed) were found for comparison with the present data. However, the present results can be compared to the relation between z_c and Froude number proposed by Noblesse *et al.* (2006),

$$\frac{z_c g}{U^2} \frac{\cos \alpha_E}{\tan \alpha_E} = \frac{2.2}{1 + F_T}, \tag{3.1}$$

where α_E is the equivalent entrance angle of the bow shape at the water line given by their equation (16) and $F_T = U/\sqrt{gT}$ with T being the effective keel depth of the model given by their equation (17). In these equations, the values of α_E and T represent weighted averages of the quantity in question via an integration from the stem to the location (X_b) of the peak of the contact point curve. In Noblesse *et al.* (2006), an empirical equation (their equation (11)) based on ship model data was used to determine X_b; however, in the present work, the measured equivalent streamwise distance to the contact point peak was used. This was necessary, since the non-standard shape of the stem region in the 2D+T wavemaker motion as depicted in figure 6(*a*) is so different from that of the models upon which equation (11) from Noblesse *et al.* is based. The values of α_E used in the present data range from 9.6° at the lowest Froude number to 10.7° at the highest Froude number and are given in table 1 along with the values of X_b, T and F_T. In figure 15(*b*), the theoretical curve of Noblesse *et al.* (2006), three-dimensional ship model data taken from figure 2 of Noblesse *et al.* (2006) (which is from experiments with ship models without bulbous

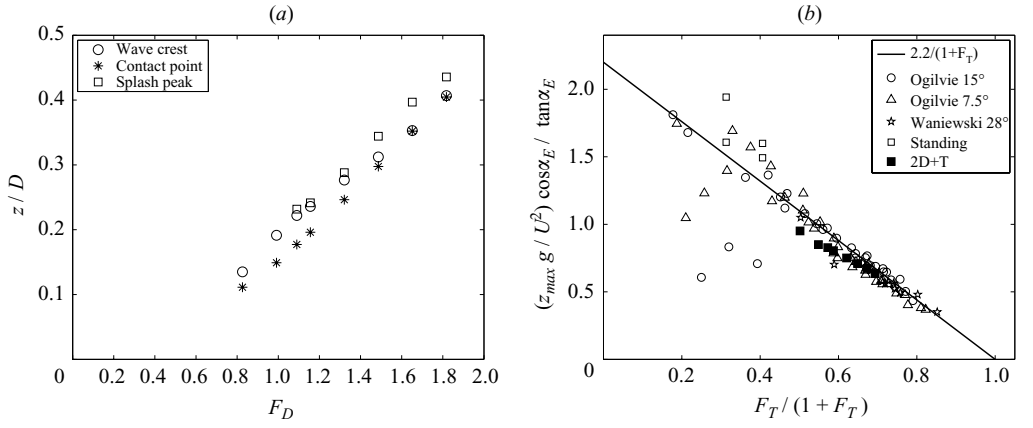

FIGURE 15. (*a*) The maximum height of the water surface contact point ($(z_c)_{max}/D$), the maximum wave height ($(z_w)_{max}/D$) and the maximum height of the splash ($(z_s)_{max}/D$) versus the draft-based Froude number $F_D = U/\sqrt{gD}$. (*b*) The maximum dimensionless contact line height ($z_c g/U^2 \cos\alpha_E/\tan\alpha_E$, where α_E is the bow entrance angle) versus the Froude number parameter $F_T/(1+F_T)$, where $F_T = U/\sqrt{gT}$ and T is the effective keel depth of the bow region. Values of α_E, T and F_T can be found in table 1. The theoretical curve is from Noblesse *et al.* (2006), and the data from tests with three-dimensional models (extracted from figure 2 of Noblesse *et al.* 2006) are from Ogilvie (1972), Standing (1974) and Waniewski, Brennen & Raichlen (2002).

bows) and the present data from figure 15 are plotted. As can be seen in the plot, the 2D+T data fall within the scatter of the three-dimensional ship model data and approach (3.1) with increasing F_T.

3.3.2. *Wave crest*

Figure 16 is a plot of the dimensionless height (z_{max}/D) of the highest point on the water surface versus t/T_{wm} for the eight values of F_D. Initially, the highest point on the water surface is the contact point, so the curves in figure 16 follow those in figure 14 for small t/T_{wm}. At about the time when the contact point z_c reaches its maximum value and begins to fall, z_{max} either levels off or continues to rise for a short time before levelling off. These transitions, which can be seen by comparing figures 14 and 16, occur at times ranging from $0.125T_{wm}$ for the lowest Froude number to $0.25T_{wm}$ for the highest Froude number and mark the beginning of the formation of the first wave crest. The curves of z_{max} versus time end when the first wave crest begins to drop in height and disappears as the splash forms; the splash eventually becomes the highest point on the profile, but these data are not shown in figure 16 (see discussion below).

Figure 17(*a*) shows the horizontal (y) position of the highest point on the wave profile versus t/T_{wm} for various equivalent ship speeds. The y coordinate is non-dimensionalized by $U_m^2/2g$ in order to spread out the data for the various Froude numbers at later times when the highest point on the wave profile is the wave crest (see above). As can be seen from the figure, at these late times the curves form straight lines, indicating a constant phase speed for each wave crest. It should also be pointed out that if the data were plotted on y-versus-x (where $x = Ut$) axes, the data for each Froude number would form the wave crest line as seen looking vertically down on the ship model as it travels from right to left with $y = 0$ being the centreline of the equivalent three-dimensional ship model. The 2D+T calculations of

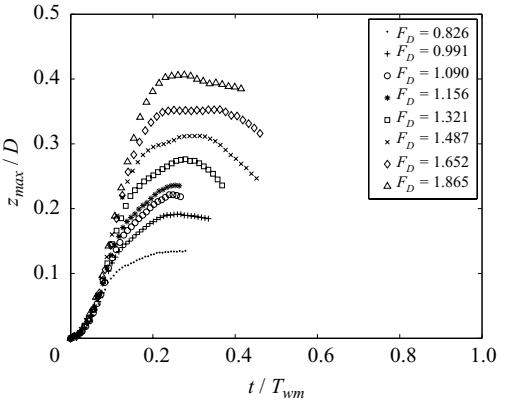

FIGURE 16. The maximum dimensionless height z_{max}/D of the water surface versus dimensionless time (t/T_{wm}) for eight Froude numbers F_D.

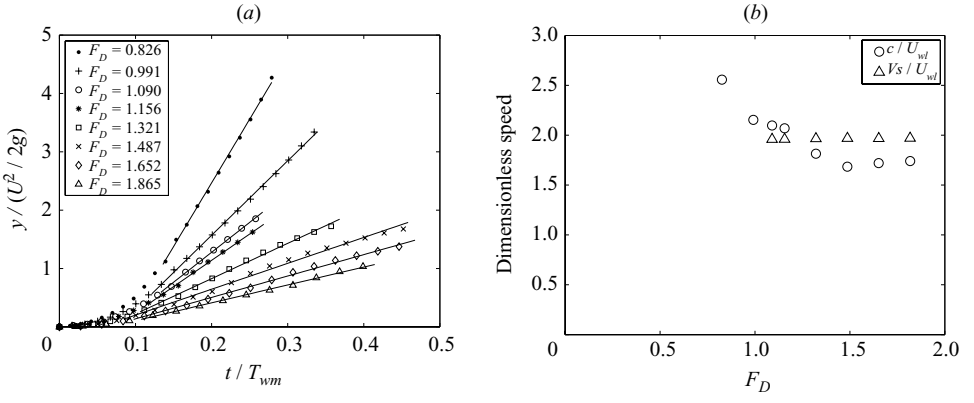

FIGURE 17. (*a*) Dimensionless horizontal position $(y/(U^2/2g))$ of the highest point on the water surface profile versus dimensionless time t/T_{wm} for eight Froude numbers. The Froude scaling of the y coordinate was chosen to spread the data out on the plot. (*b*) The dimensionless phase speed (c/U_{wl}) of the first crest produced by the wavemaker and the dimensionless speed of the front of the splash zone (V_s/U_{wl}) versus F_D.

Tulin & Wu (1996) indicate that for normal ship slenderness ratios (beam/length) of 0.1:0.2, the divergent bow-wave crests tend to be straight. In our experiments the slenderness of the equivalent ship is 0.13 $(B/L = 2.82/21.03)$. The crest trajectories shown in figure 17(*a*) are straight lines in agreement with the earlier calculations.

Figure 17(*b*) is a plot of the dimensionless wave phase speed c/U_{wl} versus F_D. (The corresponding values of c/U can be obtained by dividing the values of c/U_{wl} by 4.165.) The phase speeds were obtained from the slopes of the straight portion of the curves in figure 17(*a*). As can be seen in figure 17(*b*), c/U_{wl} drops from 2.56 to 1.68 as F_D increases from its lowest value (0.826) to 1.487, the lowest Froude number for which a plunging breaker appears. From this point, c/U_{wl} increases only slightly, reaching 1.74 at the highest Froude number. It should be noted that c/U_{wl} at the lowest Froude number is about equal to 1.0 plus c/U_{wl} at the highest Froude number. Thus, the data are consistent with the idea that the first wave produced by the wavemaker propagates in the current field of the wavemaker and has a speed relative to still water that is about equal to $1.7U_{wl}$ at all Froude numbers. Thus, at

the lower Froude numbers at which the wave has an effectively short wavelength compared to the depth ($\approx D$) of the surface current field, the wave phase speed is equal to $1.6U_{wl}$ plus the surface current whose speed is roughly U_{wl}. At the higher Froude numbers at which the wave has an effectively long wavelength, the surface current has little effect on the wave phase speed. Since the waves produced by the wavemaker do not contain a full wavelength, it is difficult to determine a wavelength from the measurements for each Froude number. However, it is interesting to note that at $F_D = 1.487$, the wavelength corresponding to the wave phase speed $1.7U_{wl}$ in still water is 2.12 m, i.e. a little more than two times the draft.

3.3.3. *Plunging jet*

In the cases with plunging breakers (the three highest Froude numbers), the motion of the tip of the plunging jet was tracked in time, and the resulting data are presented in figure 18. The dimensionless horizontal (y_j/B) and vertical (z_j/D) positions of the jet tip versus dimensionless time (t/T_{wm}) are given in figure 18(a, b), respectively. The three y_j–t data sets in figure 18(a) form nearly the same straight line, while the three z_j–t data sets in figure 18(b) form three separate curves. As can be seen in figure 18(b), the jet tip trajectory is initially upward rather than horizontal, as it would be in a typical open-water plunging breaker. In individual movie frames (see figure 12b, c), the wave profiles look similar to those of plunging breakers in deep (e.g. Bonmarin 1989; Rapp & Melville 1990) or shallow water (e.g. Miller 1976) with the shape of the jet appearing as though it is moving horizontally out of the wave crest and then falling vertically. The apparent discrepancy between the jet tip trajectory and the appearance of individual movie frames is an indication that, as one might expect, the water surface extending from the wave board to a relatively large distance away is rising as the plunging jet is formed, contributing to both the vertical motion of the crest and the jet tip. Also, it should be noted that in the present case, the jet is forming well before the wave crest leaves the wave board, and therefore it is not surprising that the jet behaves differently than in a wave breaking in open water. The solid lines going through the z_j/D versus t/T_{wm} data for each Froude number in figure 18(b) are parabolas obtained by least squares fit to the data. The combination of the linear fit to the horizontal position data (constant horizontal velocity) and parabolic fit to the vertical position data (constant vertical acceleration) is indicative of a ballistic trajectory as one might expect for this flow. The resulting horizontal velocities (v_{yj}) and vertical accelerations (a_j) of the jet tips are plotted in figure 18(c, d), respectively. Also, plotted in figure 18(c) are the wave crest phase speeds from figure 17(b) and the jet tip speed ($(v_j)_i$) at the moment just before impact with the smooth front face of the wave. As can be seen from figure 18(c), the horizontal speed of the jet tip (v_{yj}) is a little greater than the wave crest speed as one would expect. Analysis of the data indicates that $(v_{yj} - c)/c = 0.154$, 0.101 and 0.097 for $F_D = 1.487$, 1.652 and 1.817, respectively. These values are comparable to those measured in experiments on deep-water plunging breakers created by a narrowing channel width by Van Dorn & Pazan (1975), where a value of 0.08 was reported. However, values from the literature vary widely and include $(v_{yj} - c)/c = 0.32$–1.59 for numerical potential flow calculations of breakers in shallow water by New, McIver & Peregrine (1985) and $(v_{yj} - c)/c = 0.45$–0.76 for numerical viscous flow calculations of short wavelength, surface-tension-dominated breakers (Chen & Kharif 1999).

The vertical accelerations of the jet tip were normalized by gravity and plotted versus F_D in figure 18(d). As can be seen from the plot, a_j/g increases from 0.6 to 0.78 as the Froude number increases from 1.487 to 1.817. It is not surprising that

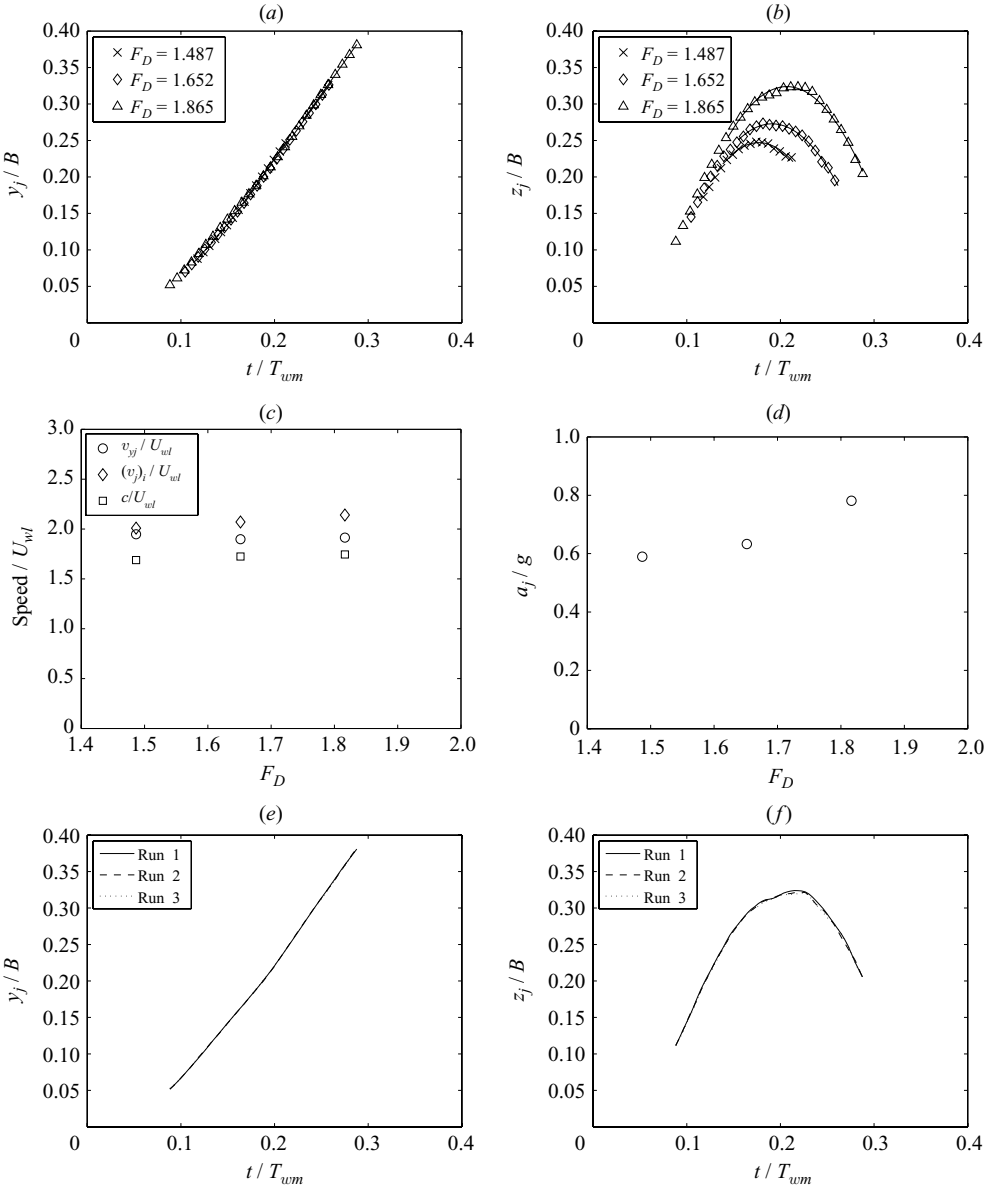

FIGURE 18. Kinematics of the jet tip for the three highest Froude numbers, $F_D = 1.487$, 1.652 and 1.817. Plunging jets did not occur at the other five Froude numbers. (*a*) Horizontal position (y_j/B) versus t/T_{wm}. (*b*) Vertical position z_j/D versus t/T_{wm}. (*c*) Dimensionless horizontal velocity component (v_{yj}/U_{wl}) and speed at impact ($(v_j)_i/U_{wl}$) of the jet tip along with the wave crest speed (c/U_{wl}) versus F_D. (*d*) Vertical acceleration of the jet tip non-dimensionalized by the gravitational acceleration (a_j/g) versus F_D. (*e*),(*f*) Plots of y_j/B and z_j/D, respectively, versus t/T_{wm} for three runs at $F_D = 1.817$.

the vertical acceleration is different from the acceleration of gravity, since the jet tip is a geometrical feature of the surface rather than the centre of mass of a material body. It is likely that the jet tip is deforming due to the effect of surface tension as it falls. As the Froude number becomes larger, the jet grows in thickness, and the effect

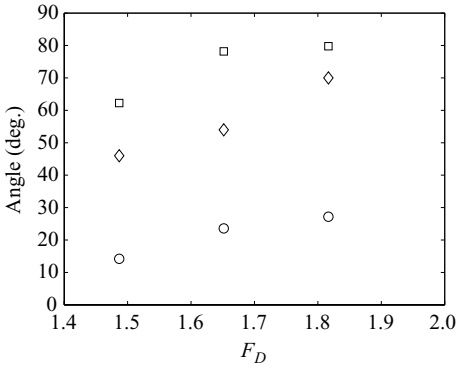

FIGURE 19. Jet tip incidence angles relative to horizontal versus Froude number ($F_D = U/\sqrt{gD}$): ○, angle of the jet tip velocity at impact in the laboratory reference frame; ◇, angle of the jet centreline as measured from photographs; □, angle of the jet tip velocity at impact as measured in the referencee frame fixed with respect to the crest.

of surface tension is probably reduced. Thus, the acceleration tends towards g with increasing Froude number.

The repeatability of the jet tip trajectory data was determined by analysis of the three runs at $F_D = 1.817$. Plots of y_j/B and z_j/D versus t/T_{wm} for these cases are shown in figure 18(e,f), respectively. As can be seen from the figures, the jet tip trajectories are highly repeatable. Analysis of this data resulted in $a_j/g = 0.796$, 0.782 and 0.769 for the three runs. The range of the values is only about $\pm 1.5\,\%$ of the mean.

Figure 19 contains a plot of the jet incidence angle at the time of impact versus F_D. Three separate measures of this angle are shown in the figure: the angle of the jet tip velocity relative to the horizontal in the laboratory reference frame, the angle of the jet centreline relative to horizontal as measured from the image of the jet impact from the high-speed movie photograph and the angle of the jet tip velocity at impact relative to the horizontal as measured in the reference frame fixed with respect to the wave crest. As seen in the figure, all three angles increase with F_D. The angles measured from the jet tip velocity are of the order of 20° in the laboratory reference frame and 80° in the reference frame of the crest. The angles measured from the single images at the time of jet impact are in between the two angles measured from the jet tip velocity.

3.3.4. *Splash*

In this subsection, the behaviour of the splash is explored. As mentioned above, the splash is here defined as the two-phase turbulent flow region created on the upstream slope of the spiling breakers or upstream of the jet impact site at the three highest Froude numbers. Obtaining the free-surface profile of the splash is difficult because of the poorly defined free surface of this air–water mixture. The only reliable quantities that could be measured were the maximum height of the splash peak, the location of the leading edge of the splash and, at least for early times, the back edge of the splash. (At later times the roughness of the water surface at the back end of the splash decays slowly, making this boundary difficult to identify.) Figure 20(a) shows the maximum height of the splash versus t/T_{wm} for the six highest Froude numbers. As can be seen from the plot, the height of the splash at first increases with time and then decreases. The maximum height of each curve increases with increasing Froude number. The splash height for the five highest Froude numbers are plotted in figure 15(a) along with the previously described data for the maximum contact point

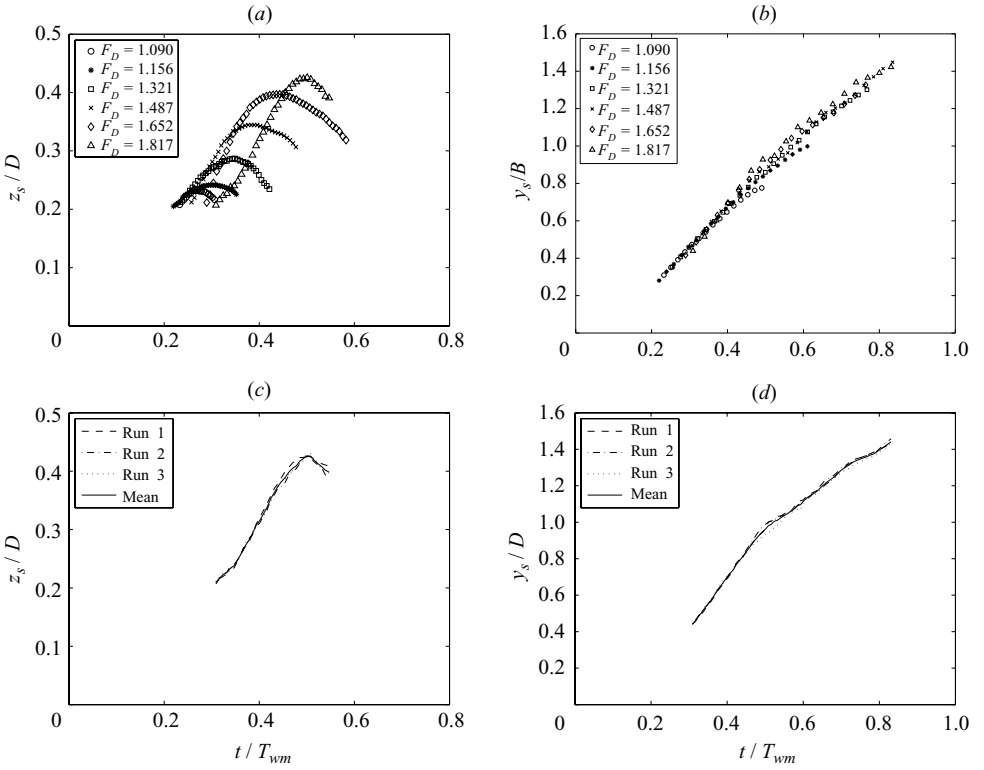

FIGURE 20. Kinematics of the splash for the six highest Froude numbers. Breaking did not occur at the other two Froude numbers. (*a*) The height of the splash peak z_s/D versus t/T_{wm}. (*b*) The horizontal position of the toe of the splash (y_s/B) versus t/T_{wm}. (*c*) Plot of z_s/D of the splash peak versus t/T_{wm} for three runs at $F_D = 1.817$. (*d*) Plot of y_s/B of the toe of the splash versus t/T_{wm} for three runs at $F_D = 1.817$.

height and the maximum wave height. As can be seen from the plot, the maximum splash height is somewhat larger than the maximum height of the wave crest for the plunging breakers ($(z_s - z_c)/z_c = 0.11$, 0.13 and 0.09, for $F_D = 1.487$, 1.652 and 1.817, respectively) and about equal to the maximum height of the wave crest for the three spilling breakers. The curve of maximum splash height versus Froude number in figure 15(*a*) shows no indication of the boundary between spilling and plunging.

Plots of the dimensionless horizontal position (y_s/B) of the leading edge of the splash versus dimensionless time (t/T_{wm}) for individual runs at the six highest Froude numbers are given in figure 20(*b*). Each curve is essentially a wobbly straight line with positive slope, though the slope does diminish somewhat at the end of each curve. The corresponding horizontal velocity of the splash leading edge (V_s) was obtained by fitting a straight line to each of the six data sets in the figure, and the results are plotted versus Froude number (along with the wave phase speed data) in figure 17(*b*). As can be seen in the plot, V_s/U_{wl} has nearly the same value of about 1.97 for all six Froude numbers. This value is a little less than the wave crest speed c for $F_D = 1.090$ and 1.156 but higher than c for the four highest Froude numbers.

Figure 21 shows the dimensionless horizontal width of the splash (W_s/B) versus dimensionless time for the four highest Froude numbers. This width increases with time, since the leading edge moves at a speed of $1.97U_{wl}$, while the back end of the

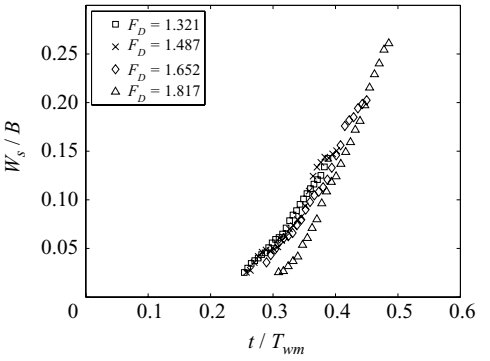

FIGURE 21. The width of the splash W_s/B versus t/T_{wm}.

splash moves relatively slowly, presumably because it represents the trailing edge of a decaying patch of free-surface turbulence. The curves end while still rising because the back end of the splash region becomes difficult to define later in the breaking process as the turbulence and free-surface fluctuations gradually decay. This difficulty also made it impossible to obtain splash width measurements at $F_D = 1.090$ and 1.156 at which the surface fluctuations at the back end of the splash zone are exceedingly small at all times.

4. Conclusions

A wavemaker with a flexible wave board was set to produce a sequence of shapes that simulated the intersection between one side of the hull of a ship model and an imaginary vertical plane oriented normal to the ship track as the ship moved at constant speed in calm water. The waves generated by this 2D+T wavemaker are simulations of the divergent bow waves produced by the equivalent three-dimensional ship model. Measurements of the histories of the water surface profiles were performed with a cinematic LIF technique at eight Froude numbers ($F_D = U/\sqrt{gD}$, where U is the forward speed of the equivalent three-dimensional ship model, g the acceleration of gravity and D the ship model draft) ranging from 0.826 to 1.817. In all cases, the water surface first rises along the wave board and then falls at the time that the primary wave crest moves away from the wave board. Non-breaking waves were produced at the lowest two Froude numbers (0.826 and 0.991), spilling breakers at the next three Froude numbers (1.090, 1,156 and 1.321) and plunging breakers at the three highest Froude numbers (1.487, 1.652 and 1.817). Various geometric characteristics of the water surface including the hull contact line, the wave crest, the plunging jet and the splash zone were measured. The curve of maximum height of the contact point as a function of F_D is in quantitative agreement with measurements by other researchers in experiments with three-dimensional ship models. The maximum height of the contact point, the maximum height of the wave crest and the maximum height of the splash all increase monotonically with F_D in more or less a linear fashion. The maximum height of the splash is about equal to the maximum height of the wave crest for the spilling breakers but is greater than the crest height for the plunging breakers. The phase speed of the primary wave changes from about $2.6U_{wl}$ at the lowest Froude number to about $1.7U_{wl}$ for the three highest Froude numbers, where U_{wl} is the maximum horizontal speed of the wave board along the height of the undisturbed water level ($U_{wl} = 0.240U$). In the cases with plunging breakers, the

jet tip velocity is initially upward and away from the wave board. The horizontal velocity of the jet tip relative to the wave crest ranges from about 15 % to 10 % of the wave crest speed. The vertical trajectory of the jet tip is parabolic, and the vertical acceleration ranges from $0.6g$ at $F_D = 1.47$ to $0.8g$ at $F_D = 1.817$. Values of vertical acceleration less than g are consistent with the jet tip being a geometrical point rather than a centre of mass and the possibility that surface tension may be causing the jet tip to contract as it falls. The effect of surface tension is expected to be stronger at the lower Froude numbers at which the jet appears to be thinner. The leading edge of the splash moves faster than the wave crest with a speed of $1.97U_{wl}$ in all cases.

The support of the Office of Naval Research (grant N000140110868, scientific officer Dr P. Purtell) is gratefully acknowledge. The authors would like to thank Eric Maxeiner, Jessica Walters and Peter Kang for their assistance during the image processing and data analysis. The wavemaker was designed and constructed by MTS, Inc., under the direction of Mr John Bushey.

REFERENCES

Baba, E. 1969 A new component of viscous resistance of ships. *J. Soc. Nav. Arch. Jpn* **125**, 9–34.

Bonmarin, P. 1989 Geometric properties of deep-water breaking waves. *J. Fluid Mech.* **209**, 405–433.

Chen, G. & Kharif, C. 1999 Two-dimensional Navier–Stokes simulation of breaking waves. *Phys. Fluids* **11** (1), 121–133.

Dommermuth, D. G., O'Shea, T. T., Wyatt, D. C., Ratcliffe, T., Weymouth, G. D., Hendrikson, K. L., Yue, D. K.-P., Sussman, M., Adams, P. & Valenciano, M. 2007 An application of Cartesian-grid and volume-of-fluid methods to numerical ship hydrodynamics. In *Ninth International Conference on Numerical Ship Hydrodynamics*, Ann Arbor, MI.

Dommermuth, D. G., O'Shea, T. T., Wyatt, D. C., Sussman, M., Weymouth, G. D. & Yue, D. K. P. 2006 Numerical simulation of ship waves using Cartesian-grid and volume-of-fluid methods. In *26th Symposium on Naval Hydrodynamics*, Rome, Italy.

Dong, R. R., Katz, J. & Huang, T. T. 1997 On the structure of bow waves on a ship model. *J. Fluid Mech.* **346** 77–115.

Landrini, M., Colagrossi, A. & Tulin, M. P. 2001 Breaking bow and stern waves: numerical simulations. In *16th International Workshop on Water Waves and Floating Bodies*, Hiroshima, Japan.

Longuet-Higgins, M. S. 1995 On the disintegration of the jet in a plunging breaker. *J. Phys. Oceanogr.* **25** (10), 2458–2462.

Miller, R. L. 1976 Role of vortices in surf zone prediction: sedimentation and wave forces. In *Beach and Nearshore Sedimentation*, pp. 92–113. Society of Economic Paleontologists and Mineralogists, ed. R. A. Davis and R. L. Ethington.

Miyata, H. & Inui, T. 1984 Nonlinear ship waves. *Adv. Appl. Mech.* **24**, 215–288.

New, A. L., McIver, P. & Peregrine, D. H. 1985 Computations of overturning waves. *J. Fluid Mech.* **150**, 233–251.

Noblesse, F., Delhommeau, G., Guilbaud, M., Hendrix, D. & Yang, C. 2008 Simple analytical relations for ship bow waves. *J. Fluid Mech.* **600**, 105–132.

Noblesse, F., Hendrix, D., Faul, L. & Slutsky, J. 2006 Simple analytical expressions for the height, location, and steepness of a ship bow wave. *J. Ship Res.* **50**, 360–370.

Ogilvie, T. F. 1972 The wave generated by a fine ship bow. In *Proceedings of the Ninth Symposium on Naval Hydrodynamics* (ed. R. Brard & C. Castera), pp. 1483–1524. Department of the Navy.

Olivieri, A., Pistani, F., Wilson, R., Campana, E. F. & Stern, F. 2007 Scars and vortices induced by ship bow and shoulder wave breaking. *J. Fluids Engng* **129**, 1445–1459.

Rapp R. J. & Melville W. K. 1990 Laboratory measurements of deep-water breaking waves. *Phil. Trans. R. Soc. Lond.* A **331**, 735–800.

Shakeri, M. 2005 An experimental 2D+T investigation of breaking bow waves. PhD dissertation, Department of Mechanical Engineering, University of Maryland, MD.

Shakeri, M., Maxeiner, E., Fu, T. & Duncan, J. H. 2009 An experimental examination of the 2D+T technique. *J. Ship Res.* **53**(2), 59–71.

Song, W. & Maruo, H. 1993 Bow impact and deck wetness: simulations based on nonlinear slender body theory. In *Proceedings of the Third International Offshore and Polar Engineering Conference*, vol. 3, pp. 34–38. Publisher: International Society of Offshore and Polar Engineers.

Standing, R. G. 1974 Phase and amplitude discrepancies in the surface wave due to a wedge-ended hull form. *J. Fluid Mech.* **62** 625–642.

Tulin, M. P. 1957 The theory of slender surface planing at high speeds. *Schiffstechnik, 4, Heft* **21**, 125–133.

Tulin, M. P. & Hsu, C. C. 1986 Theory of high speed displacement ships with transom sterns. *J. Ship Res.* **21-1**.

Tulin, M. P. & Wu, M. 1996 Divergent bow waves. In *Proceedings of the 21th Symposium on Naval Hydrodynamics*, pp. 661–679.

Van Dorn, W. G. & Pazan, S. E. 1975 Laboratory investigation of wave breaking. Part 2. Deep water waves. *Rep.* 75-21. Scripps Institution of Oceanography. *Rep.* 71. Advanced Ocean Engineering Laboratory.

Waniewski, T. A., Brennen, C. E. & Raichlen, F. 2002 Bow wave dynamics. *J. Ship Res.* **46**, 1–15.